ACS APPLIED MATERIALS & INTERFACES

Research Article

www.acsami.org

Growth Control of MoS_2 Nanosheets on Carbon Cloth for Maximum Active Edges Exposed: An Excellent Hydrogen Evolution 3D Cathode

Nan Zhang,[†,‡] Shiyu Gan,[†] Tongshun Wu,*[,†] Weiguang Ma,[†,‡] Dongxue Han,[†] and Li Niu[†]

[†]State Key Laboratory of Electroanalytical Chemistry, c/o Engineering Laboratory for Modern Analytical Techniques, Changchun Institute of Applied Chemistry, Chinese Academy of Sciences, Changchun 130022, Jilin, China

[‡]University of the Chinese Academy of Sciences, Beijing 100039, China

Supporting Information

ABSTRACT: To greatly improve the hydrogen evolution reaction (HER) performance, it is the key approach to expose as many active edges of MoS_2 as possible. This target is the research hotspot and difficulty of MoS_2 which is a promising HER catalyst. In this work, we realized the active-edges control of MoS_2 nanosheets on carbon cloth (CC) by growth control during the synthesis procedure. Moreover, MoS_2 nanosheets vertically grown on carbon cloth (MoS_2⊥CC) was confirmed to be the best morphology with maximum active edges exposed. Multifactors structure control resulted in abundant active-edges exposure and effective electron delivery, thus excellent HER activity. This three-dimensional cathode, MoS_2⊥CC, can reach a great current density of 200 mA/cm^2 at a small overpotential of 205 mV. The preeminent HER performance can rival the best MoS_2-based catalyst ever reported.

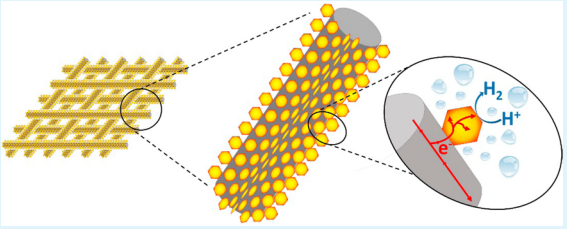

KEYWORDS: *active-edges control, vertical alignment, three-dimensional, MoS_2 nanosheets, hydrogen evolution reaction*

1. INTRODUCTION

Hydrogen is clean and sustainable. It can solve the stress situation brought by pollution to the environment and the increasing energy demands.[1−3] Electrochemical splitting of water is a remarkable technique for its abundant source, clean technique, and high purity production of hydrogen.[4] Although noble Pt-group metals are the most efficient electrocatalyst for hydrogen evolution reaction (HER),[5,6] their high cost and resource scarcity hinder the application. MoS_2, which is abundant at lower cost, has been considered as one of the most promising catalysts since its hydrogen binding energy is close to that of Pt-group metals by density functional theory calculations.[7] However, to achieve ideal catalytic activity of MoS_2, two main challenges need to be overcome. First, the HER active sites have been identified to arise from the edges, rather than the basal planes of MoS_2 sheet by theoretical calculations and experimental studies.[8] To expose more edges, defect-rich MoS_2,[9] oxygen-incorporated MoS_2,[10] and three-dimensional (3D) porous MoS_2 have been synthesized.[11] Second, the poor conductivity of MoS_2 limits the electron transfer and encumbers the electrocatalytic efficiency to HER. To solve this problem, Lukowski and Voiry have successfully exfoliated 1T-MoS_2 as metallic MoS_2 with high conductivity.[12,13]

Many kinds of carbon materials have been employed to synthesize MoS_2-based catalysts to conquer these two challenges simultaneously, for example, carbon nanotubes (CNTs),[14] graphene,[15,16] carbon fibers,[17] amorphous carbon,[18] and so on. They can not only improve the electron delivery but also enfold MoS_2 for great active-edges exposure against their trend of curling up into inorganic fullerene structures.[19] Although MoS_2 of different morphologies have been synthesized and supported on kinds of high-conducting materials, the HER activity of MoS_2-based material is not satisfactory yet. The exposed active-edge sites should be further enlarged and electron transfer efficiency should be further improved. In this way, some substrates, such as mesoporous graphene,[20] crumpled graphene balls,[21] as well as CNT and graphene together,[22] have been designed to construct 3D structures with more active edges exposed. Herein, commercially available carbon cloth (CC) was chosen to be the substrate for MoS_2 to form such a 3D cathode. CC has been widely employed in electric fields of different applications for their low cost, excellent conductivity, good physical strength, and high flexibility.[23−25] Meaningfully, the use of CC helped to integrate the electrode into devices for applications.

In this work, active-edges control of MoS_2 nanosheets grown on CC was realized by growth control during the synthesis procedure for the first time. This investigation was pursued from morphology to profound growth mechanism, which builds a comprehensive understanding of the impact of active-edges control on HER performance. In this research, vertical alignment of MoS_2 on CC (MoS_2⊥CC) was proved to be the optimum morphology with maximum active-edges exposure. More importantly, preeminent HER performance has been achieved by MoS_2⊥CC. Two main reasons

Received: March 24, 2015
Accepted: May 17, 2015
Published: May 17, 2015

DOI: 10.1021/acsami.5b02586
ACS Appl. Mater. Interfaces 2015, 7, 12193−12202

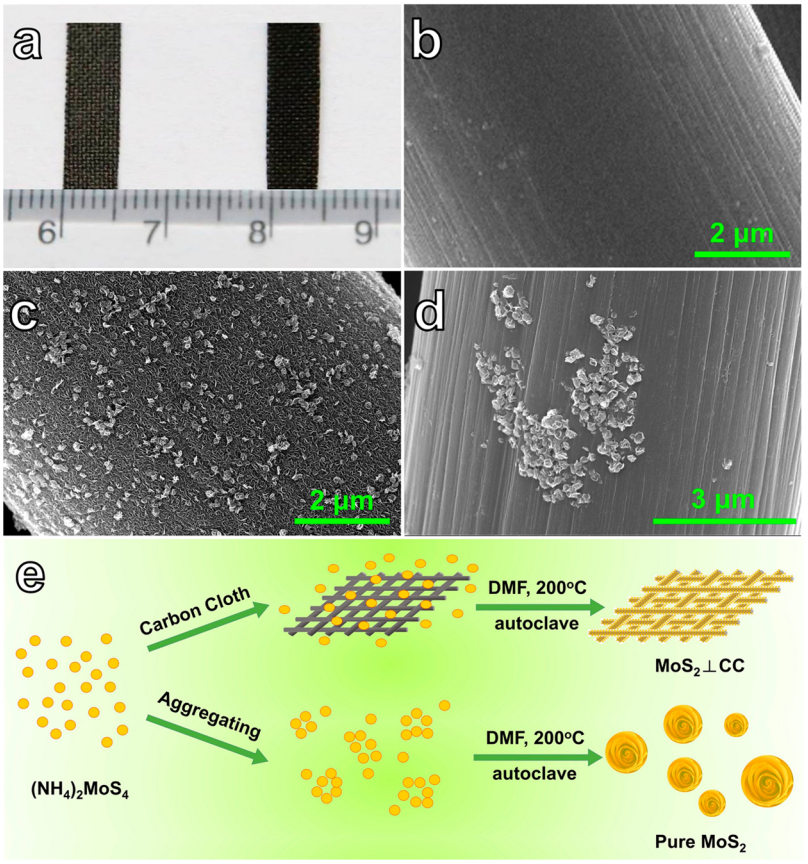

Figure 1. (a) Photographs of blank CC on the left and MoS_2⊥CC on the right. SEM images of (b) blank CC, (c) MoS_2⊥CC, and (d) MoS_2-CC. (e) Schematic solvothermal synthesis of MoS_2⊥CC with CC and pure MoS_2 without CC.

contributed to the outstanding HER performance. First, vertically and densely aligned MoS_2 nanosheets on CC can expose almost edges all-around of every MoS_2 nanosheet and, therefore, exposed maximum active sites to the electrolyte. Second, the electron transfer efficiency was improved by the involvement of high conductive CC, and the direct and effective electron delivery from CC to vertically aligned MoS_2 nanosheets further. Above all, to the best of our knowledge, it is the top highest HER efficient catalyst among MoS_2-based electrocatalysts ever reported.

2. EXPERIMENTAL SECTION

2.1. Materials. CC was purchased from Phychemi (Hong Kong) Company Limited. $(NH_4)_2MoS_4$, Pt/C (20 wt %), and Nafion solution (5 wt %) were bought from Sigma-Aldrich. *N*,*N*-Dimethylformamide (DMF), ethylene glycol (EG), acetone, and ethanol were obtained from Beijing Chemicals Corporation, China. Unless otherwise stated, reagents were of analytical grade and used as received. The water used throughout all experiments was doubly distilled water from a Millipore system (>18 MΩ cm).

2.2. Preparation of MoS_2⊥CC. CC was cleaned by sonication sequentially in acetone, water, and ethanol for 10 min each. The cleaned CC (3 cm × 3 cm) was immersed in 30 mL of DMF solution containing 29.36 mg of $(NH_4)_2MoS_4$ and stirred for 30 min. Then, the solution and CC were transferred into a 50 mL Teflon-lined stainless autoclave and kept at 200 °C for 15 h. After it naturally cooled at room temperature, MoS_2⊥CC was taken out from the autoclave and rinsed thoroughly with water and ethanol successively several times and then dried in an oven at 70 °C for 10 h. The loading for MoS_2 on CC was determined to be 0.27 mg/cm^2 via a high-precision microbalance. In control experiments, different experimental conditions was employed, respectively, as following: (a) solvent contrast: DMF, water, and EG; (b) temperature contrast: 180, 200, 220, and 240 °C; (c) concentration contrast: 45, 29.36, 14.7, and 7.35 mg of $(NH_4)_2MoS_4$.

Pure MoS_2 was synthesized by the similar method without adding CC in the autoclave and collected by centrifugation.

2.3. Preparation of Physically Mixed MoS_2 with CC (MoS_2-CC) and Pt/C with CC. Pt/C and pure MoS_2 were loaded onto CC as working electrodes in contrast experiments. Pt/C ink was prepared by dispersing 1.4 mg of Pt/C in 1 mL of ethanol containing 35 μL of Nafion solution and treated by sonication until a homogeneous dispersion was obtained. MoS_2 ink was prepared in the same way with pure MoS_2 powder. Every working electrode in contrast experiments was fabricated by loading 50 μL of catalyst ink evenly on the effective working area of CC (0.5 cm × 0.5 cm) and drying in an oven at 70 °C for 10 h. The loading of working electrodes in contrast experiments was all 0.27 mg/cm^2, the same with that of MoS_2⊥CC. Pt/C is used as the abbreviation of physically mixed Pt/C with CC henceforth.

2.4. Characterization of MoS_2⊥CC. Images of scanning electron micrograph (SEM), scanning transmission electron microscopy (STEM), and corresponding energy-dispersive X-ray (EDX) elemental mapping images were obtained on a NOVA NANOSEM 450 FEI scanning electron microscope. Transmission electron microscopy (TEM) and high-resolution transmission electron microscopy (HRTEM) images were carried out on an FEI TECNAI G2 F20 S-TWIN transmission electron microscope operating at 200 kV. The X-ray diffraction (XRD) measurements were recorded in the range of 20−80° (2θ) on a D8 Focus diffractometer (Bruker) with Cu Kα radiation (λ = 0.154 05 nm), operated at 40 kV and 30 mA, and was applied to investigate the crystallographic structure of the as-fabricated products. X-ray photoelectron spectroscopy (XPS) analysis was carried out on an ESCALAB MKII X-ray photoelectron spectrometer with Al Kα X-ray radiation as the X-ray source for excitation.

2.5. Electrochemical Measurements. All electrochemical experiments were performed in the electrolyte of 0.5 M H_2SO_4 with a three-

DOI: 10.1021/acsami.5b02586
ACS Appl. Mater. Interfaces 2015, 7, 12193−12202

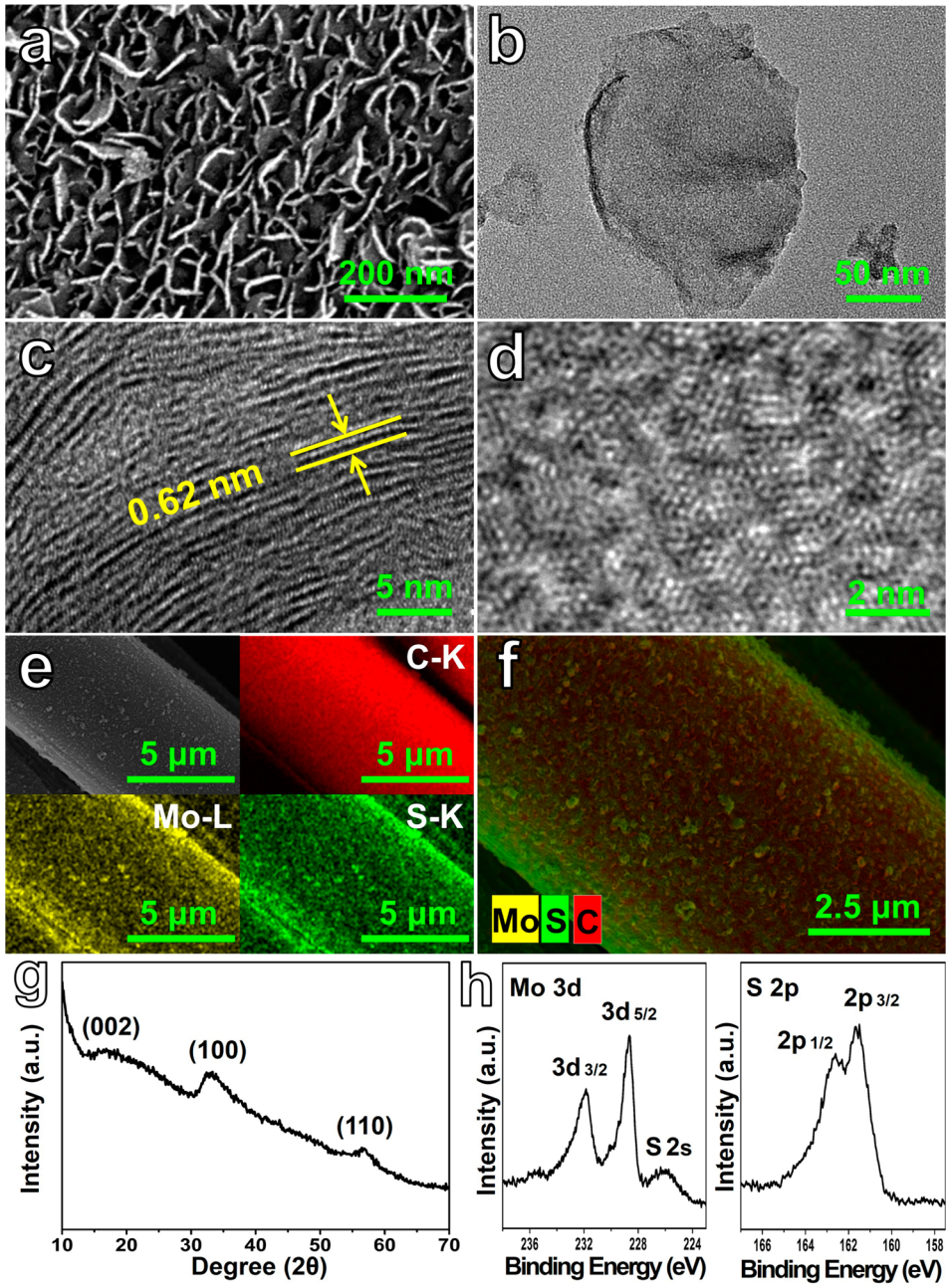

Figure 2. (a) High-magnification SEM image of MoS_2⊥CC. (b) TEM image of MoS_2 obtained from MoS_2⊥CC and (c, d) the corresponding HRTEM images. (e) STEM image and EDX elemental mapping of C, Mo, S for MoS_2⊥CC. (f) Layered EDX elemental mapping of C, Mo, S for MoS_2⊥CC. (g) XRD pattern of MoS_2. (h) XPS spectra of Mo 3d and S 2p.

electrode system. The system consisted of MoS_2⊥CC with an effective working area of 0.5 cm × 0.5 cm as the working electrode, a saturated calomel electrode (SCE) as the reference electrode, and a graphite rod as the counter electrode. When investigating the influence of MoS_2⊥CC effective working area on its HER performance, we chose 0.5 cm × 1 cm and 1 cm × 1 cm as the effective working areas, respectively. Linear sweep voltammetry (LSV) was measured with the scan rate of 5 mV/s. Cyclic voltammetry (CV) was measured with scan rates of 20, 40, 60, 80, 100, 120, 140, 160, 180, and 200 mV/s, respectively, in the potential ranging from 0.34 to 0.44 V in the investigation of electrochemical double-layer capacitances. During the investigation of stability, CV was performed for 500 cycles and then 1500 cycles with a scan rate of 100 mV/s in the potential ranging from −0.2 to 0.2 V. The amperometric *i*−*t* curve was obtained at a static overpotential of 150 mV. The measurements above-mentioned were all conducted by a CHI 760e electrochemical analyzer (CH Instruments, Inc., Shanghai). All data were *iR* corrected determined by a CHI 760e via the resistance test. Electrochemical impedance spectroscopy (EIS) measurements were carried out with a Solartron 1255B Frequency Response Analyzer (Solartron Inc., U.K.) with frequencies ranging from 100 kHz to 0.01 Hz. All the experiments were carried out without an activation process and performed at room temperature. All the data are presented relative to a reversible hydrogen electrode (RHE).

3. RESULTS AND DISCUSSION

3.1. Characterization of MoS_2⊥CC. MoS_2⊥CC was proved to achieve the optimum HER performance through active-edges control investigation (see details in section 3.3). It was successfully fabricated via the solvothermal method using DMF at 200 °C with the precursor concentration of 0.98 mg/

DOI: 10.1021/acsami.5b02586
ACS Appl. Mater. Interfaces 2015, 7, 12193−12202

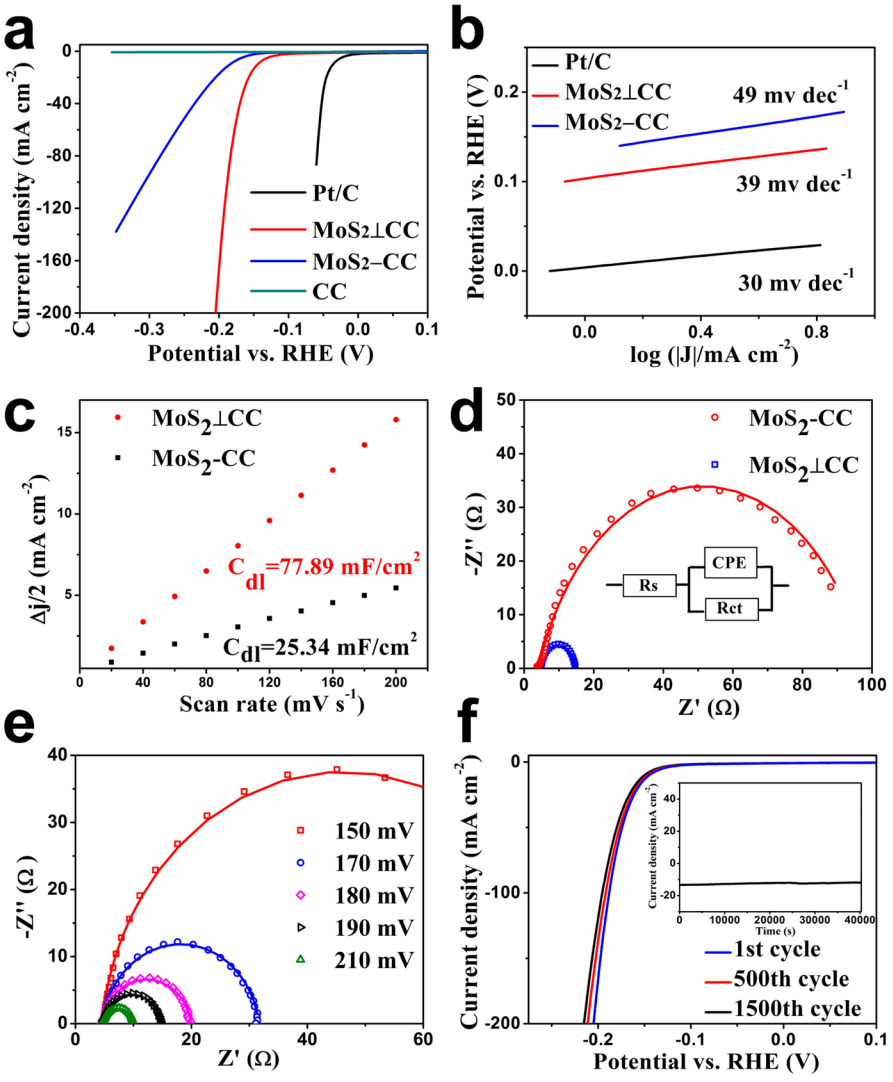

Figure 3. (a) Polarization curves of blank CC, MoS_2-CC, MoS_2⊥CC, and Pt/C. (b) Tafel plots of MoS_2-CC, MoS_2⊥CC, and Pt/C. (c) Linear fitting of the capacitive currents of the catalysts versus scan rates. (d) Nyquist plots of MoS_2⊥CC and MoS_2-CC at 190 mV overpotential. The inset circuit diagram shows the equivalent circuit model used to fit the experimental data, with empty patterns representing the experiment data and solid line for fitted curve. (e) Nyquist plots of MoS_2⊥CC cathode at different overpotentials. (f) Polarization curves for MoS_2⊥CC initially, after 500 and 1500 cycles were displayed (inset: time dependence of cathodic current density curve for MoS_2⊥CC).

mL. After grown with MoS_2, the gray color of blank CC (left) turning to black MoS_2⊥CC (right) results from the black color of MoS_2, as the photographs in Figure 1a show. Compared with the SEM image of blank CC (Figure 1b), by the solvothermal synthesis, the successful growth of MoS_2 nanosheets on CC with lots of active edges exposed is illustrated by the SEM image of MoS_2⊥CC (Figure 1c). In contrast, MoS_2 which was physically mixed with CC (Figure 1d) appears to be agglomerating clusters with large amounts of active edges buried. From this point, the solvothermal synthesis of MoS_2⊥CC is significant for the achievement of the edge-rich morphology. As shown in the synthesis procedures in Figure 1e, $(NH_4)_2MoS_4$ is reduced to edge-rich MoS_2 nanosheets grown on CC, while agglomerating pure MoS_2 are synthesized in the similar way in the absence of CC. In detail, pure MoS_2 synthesized without CC are substantiated to fold and agglomerate together. They look like rosemary buds with lots of edges buried inside due to the thermodynamically stable status according to their SEM and TEM (Figure S1a,b, Supporting Information). In the presence of CC, as exhibited in Figure 2a, MoS_2 nanosheets vertically and densely grew on CC with a large amount of edges exposed. Complementarily, the TEM image of MoS_2 (Figure 2b) shows an individual sheet obtained from MoS_2⊥CC by sonication treatment. It proves that MoS_2 nanosheets expand themselves into separated ones when grown on CC. Compared with a MoS_2 bud, each MoS_2 nanosheet grown on CC looks like an individual petal and exposes almost all the edge sites around of it, which affirms that we have successfully realized the maximization of exposed edges by CC as a perfect substrate. The 0.62 nm interlayer distance shown by the HRTEM image in Figure 2c corresponds to the (002) plane of MoS_2, and the 0.23 nm Mo−S distance (Figure 2d) corresponds to the (100) plane of MoS_2.[26] The STEM image and corresponding EDX elemental mapping images of C, Mo, and S (Figure 2e) reveal that Mo and S elements are intensively spread onto each whole carbon fiber. Furthermore, the corresponding layered EDX elemental mapping image (Figure 2f) straightforwardly and visually substantiates the dense growth of MoS_2 nanosheets all around CC.

DOI: 10.1021/acsami.5b02586
ACS Appl. Mater. Interfaces 2015, 7, 12193−12202

Table 1. Comparison of HER Performance of MoS_2⊥CC with Other MoS_2-Based Catalysts

catalyst	onset η (mV)	Tafel slope (mV dec^{-1})	current density (j, mA cm^{-2})	η at the corresponding j potential (mV)	reference
graphene-surpported MoS_2	~100	41	48	200	15
MoO_3−MoS_2 core−shell nanowires	150−200	50−60	20	272	63
mesoporous 3D MoS_2	150−200	50			11
defect-rich MoS_2	120	50	13	200	9
oxygen-incorporated MoS_2	120	55	125.6	300	10
metallic MoS_2	187	43	200	400	12
1T MoS_2	100	400			13
MoS_2 formed on mesoporous graphene	100	42	30−40	200	20
network MoS_2/CNTs composite	90	44.6	15−20	200	14
MoS_2/N-CNT forest	75	40	10	110	64
graphene-supported MoS_2 flower	190	95	~30	300	16
CNT−graphene hybrid supported MoS_2	140	100	10	255	22
layer confined MoS_2/graphene	~140	41	23	200	65
MoS_2/3D-graphene hierarchical framework	107	86.3	51.6 A/g	400	66
amorphous MoS_2/nanoporous gold	125	41	5.7	200	67
Li-MoS_2/carbon fiber paper	100	62	200	200	32
S-MoS_2 on N-doped carbon nanofibers	30	38	10	120	17
MoS_2/N-doped graphene nanosheet aerogels	236	230	10	261	68
MoS_2/amorphous carbon	80	40	91	200	18
MoS_x/graphene	130	43	17	200	30
MoS_x on crumpled graphene balls	130	51.9	220	300	21
MoS_2 perpendicular to graphene		43	10	172	28
vertically aligned MoS_2 on carbon cloth	100	39	200	205	this work

ACS Appl. Mater. Interfaces 2015, 7, 12193−12202
DOI: 10.1021/acsami.5b02586

XRD and XPS were measured to characterize the MoS_2 grown on CC. XRD pattern of MoS_2 scratched from MoS_2⊥CC (Figure 2g) shows diffraction characteristic peaks at 15.9, 32.7, and 56.8° corresponding, respectively, to the (002), (100), and (110) planes of the well-defined and hexagonally symmetric structured MoS_2. Moreover, the (002) diffraction peak of MoS_2 grown on CC is weak and broad as reported,[16,27,28] which indicates more ultrathin MoS_2 nanosheets produced with less stacking.[18,26,29] The chemical state of MoS_2 on CC was further confirmed by XPS analysis, as shown in Figure 2h. The binding energies of 228.7 and 231.9 eV are attributed to Mo $3d_{5/2}$ and Mo $3d_{3/2}$, and the binding energies of 161.6 and 162.6 eV correspond to S $2p_{3/2}$ and S $2p_{1/2}$. This indicates that Mo^{4+} and S^{2-} are the dominant states.

3.2. HER Performance of MoS_2⊥CC. Electrochemical performance of this MoS_2⊥CC 3D cathode for HER was demonstrated by LSV measurement. For comparison study, we also tested blank CC, MoS_2-CC, and Pt/C. As Figure 3a shows, Pt/C shows the best HER activity with a negligible onset overpotential, whereas blank CC hardly exhibits any HER activity in the measurement voltage range. Compared with the onset overpotential of MoS_2-CC of 140 mV, MoS_2⊥CC exhibits a much lower onset overpotential of 100 mV. Moreover, further negative potential causes a rapid rise of MoS_2⊥CC cathodic current density. At 205 mV overpotential, the current density of MoS_2⊥CC reaches 200 mA/cm^2, which is about 9 times larger than that of MoS_2-CC (20 mA/cm^2). Furthermore, this result is superior to most MoS_2-based electrocatalysts previously reported (Table 1), which verifies that MoS_2⊥CC acts as a high-performance 3D cathode for hydrogen generation.

In addition, the influence of MoS_2⊥CC effective working area on HER activity was further explored. Different currents, but the same current density, of three electrodes with different effective working areas are obtained, as shown in Figure S2 (Supporting Information). This phenomenon suggests that the HER activity is independent of the MoS_2⊥CC effective working area. It is also a significant evidence for the uniform growth of MoS_2 on CC. To realize the low cost of every fabricated cathode, we chose to use small pieces of MoS_2⊥CC electrodes with 0.5 cm × 0.5 cm as the effective working area. Even in such a little cathode, a large amount of hydrogen bubbles generated and released from it (view video in attachment).

The Tafel plots, which are recorded with the linear regions fitted into the Tafel equation, yielding Tafel slopes of 30 mV per decade for Pt/C, 39 mV per decade for MoS_2⊥CC, and 49 mV per decade for MoS_2-CC, respectively, as shown in Figure 3b. The Tafel slope of MoS_2⊥CC is also smaller than that of almost all the MoS_2-based electrocatalysts reported in recent years, as shown in Table 1, which proves the superior HER efficiency of this 3D cathode. Furthermore, the Tafel slope value can also imply the mechanism procedure of hydrogen reduction on cathodes.[15] In acid solutions, three principal reaction steps, as in the following eqs 1−3, are involved with Tafel slopes of 120, 40, and 30 mV per decade, respectively.[18,30] According to this, the Tafel slope of 39 mV per decade obtained by the MoS_2⊥CC electrode suggests that the Volmer−Heyrovsky mechanism occurred via a fast adsorption reaction (eq 1), then an electrochemical desorption reaction as the rate-determining reaction (eq 2).

$$\text{Volmer reaction: } H_3O^+ + e + \text{catalyst} \rightarrow \text{catalyst-H} + H_2O \quad (1)$$

$$\text{Heyrovsky reaction: } H_3O^+ + e + \text{catalyst-H} \rightarrow \text{catalyst} + H_2 + H_2O \quad (2)$$

$$\text{Tafel reaction: catalyst-H} + \text{catalyst-H} \rightarrow 2\text{catalyst} + H_2 \quad (3)$$

Both polarization curves and Tafel plots show excellent HER efficiency of MoS_2⊥CC, which is associated with its morphology and electronic properties. To estimate the effective electrochemically active area of MoS_2⊥CC, we employed CV measurement to measure the electrochemical double-layer capacitances (EDLCs), C_{dl}. A potential range from 0.34 to 0.44 V without faradic current was selected,[31,32] which meant that the current response in this region was attributed to the charging of the double layer.[28] CV curves were obtained at various scan rates in this region (Figure S3, Supporting Information). The halves of the positive and negative current density differences at the center of the scanning potential ranges are plotted versus the voltage scan rate in Figure 3c, in which the slopes are the EDLCs. The C_{dl} of MoS_2⊥CC is 77.89 mF/cm^2, more than 3 times of the C_{dl} of MoS_2-CC (25.34 mF/cm^2). The large electrochemically active area confirms the maximized exposed active edge sites due to the dense and vertical growth of MoS_2 nanosheets on CC.

Apart from the great active edges exposure, efficient electron transfer is also essential for excellent HER performance. As shown in Figure 3d, the Nyquist plots reveal that the charge transfer resistance (R_{ct}) of MoS_2⊥CC (10.29 Ω) is much lower than that of MoS_2-CC (93.96 Ω). This very low value corresponds to a fast charge transfer at the interface between electrocatalyst and electrolyte and results in the excellent electrocatalysis for HER. This is ascribed to the involvement of CC as a high conductive substrate to improve the conductivity of the composite. Furthermore, due to the improved effective contact between MoS_2 and CC through solvothermal synthesis, electrons can be delivered directly and efficiently from high conductive CC to vertically aligned MoS_2 nanosheets. More importantly, as reported, aligning the MoS_2 nanosheets perpendicular to conductive substrates optimizes the conductivity of the conductive substrates.[28,33] In addition, the Nyquist plots of the MoS_2⊥CC electrode at different overpotentials are shown in Figure 3e. The R_{ct} are 83.37, 27.04, 15.38, 10.29, and 5.449 Ω corresponding to 150, 170, 180, 190, and 210 mV, respectively. This illustrates more and more rapid electron transfer and electrocatalytic performance for HER with the increased overpotential, which is in agreement with the polarization curve of MoS_2⊥CC.

We further inspected the durability of the MoS_2⊥CC electrode. First, we employed CV measurement for this investigation. Figure 3f shows the polarization curves of MoS_2⊥CC before and after 500 and 1500 CV cycles. Slight decays in current density are observed, suggesting the high stability of MoS_2⊥CC. On the other hand, we employed a static 150 mV overpotential and obtained the time-dependent current density curve of MoS_2⊥CC (in the inset of Figure 3f) with slight degradation of the cathodic current degradation during this 40 000 s. It reveals the stability under HER conditions of this cathode and the strong binding of MoS_2 nanosheets with CC. Furthermore, the cathode is proved to be robust since no

DOI: 10.1021/acsami.5b02586
ACS Appl. Mater. Interfaces 2015, 7, 12193−12202

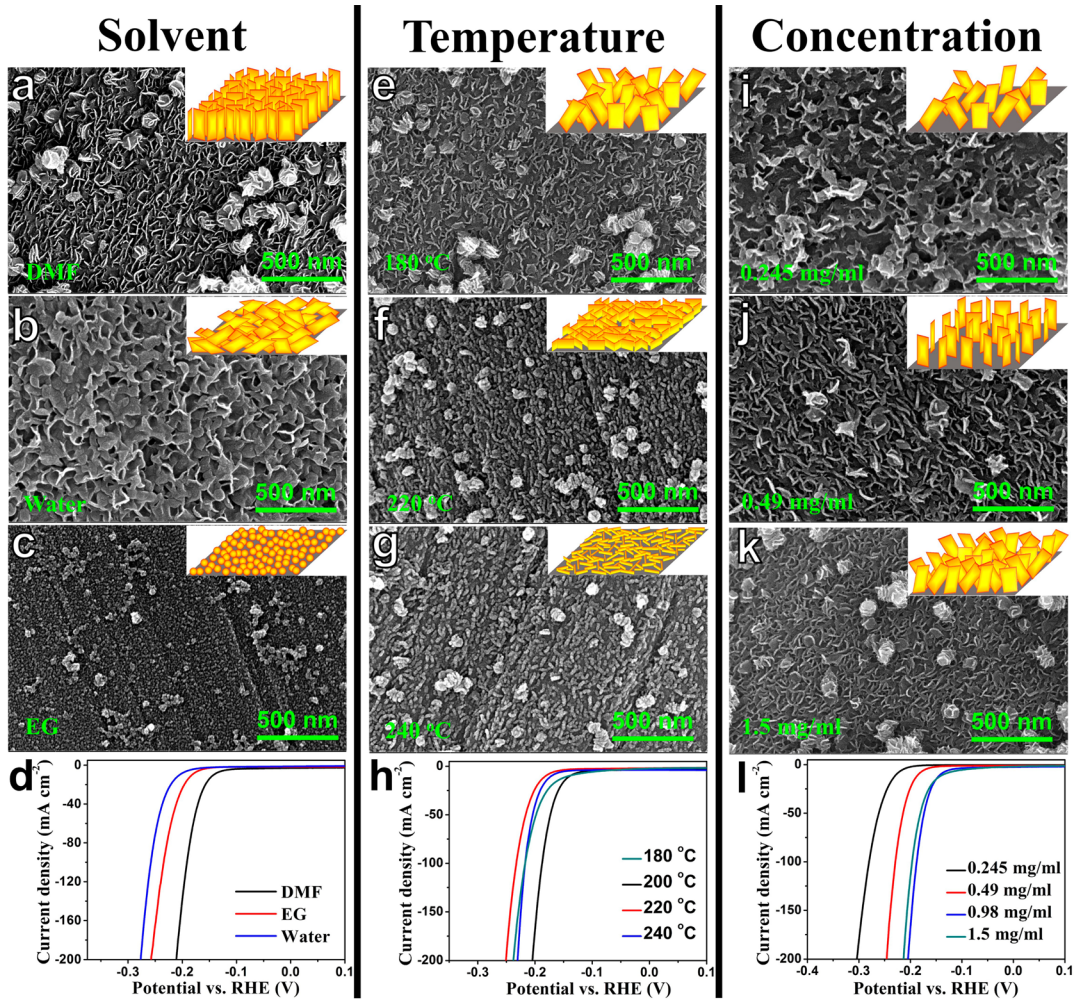

Figure 4. SEM images of MoS_2 on CC fabricated using (a) DMF, (b) water, (c) EG, (e) 180 °C, (f) 220 °C, (g) 240 °C, (i) 0.245 mg/mL, (j) 0.49 mg/mL, (k) 1.5 mg/mL and their corresponding polarization curves (d, h, l).

change has been observed before (Figure S4a, Supporting Information) and after 30 min sonication treatment of MoS_2⊥CC (Figure S4b), according to their SEM images. Overall, these durable tests substantiate the successful fabrication of this stable and robust MoS_2⊥CC 3D cathode.

3.3. Active-Sites Control. Active-sites control is indispensable for a decent HER performance. As reported, the exposure of active edges can be controlled by adjusting the morphology of MoS_2.[34,35] Different solvothermal conditions were applied here to realize the active-edges control, which was further convinced by polarization curves. During the synthesis progress, the main effectors to the morphologies of products are solvent,[36−39] temperature,[40−43] and concentration.[43−48] Furthermore, growth mechanisms of different synthesis conditions were analyzed here in order to take a profound insight of the active-edges control in this investigation.

First, we investigated the solvent effect of DMF, water, and EG in the solvothermal procedure, respectively. As Figure 4a shows, MoS_2 nanosheets densely and vertically grown on CC with great active edges exposed as the optimum morphology have been synthesized using DMF at 200 °C with the precursor concentration of 0.98 mg/mL. However, when water is applied as solvent, sparse MoS_2 nanosheets slump over CC and attach with each other (Figure 4b). As Xu et al. suggested, the lower saturated pressure of water which attributes to the lower boiling point contributes to a slower growth and larger size.[37] Therefore, MoS_2 nanosheets synthesized in water were larger than those synthesized in DMF.[39] Consequently, a strong interfacial attractive force between substrates and MoS_2 influenced the morphology of MoS_2 on CC and contributed to the slant of nanosheets.[14,18,49]

When EG was used as solvent, MoS_2 appeared to be little balls rather than nanosheets (Figure 4c). EG has been used in many solvothermal syntheses as both solvent and reducing agent.[45,50,51] $(NH_4)_2MoS_4$ was reduced to MoS_2 by EG in our experiment. As reported, EG was found to bring a decrease of the product size and the capping ability of EG helped to reduce exposed areas and form compact structures.[36,52] Accordingly, the small size and compact nanosphere structure of MoS_2 attributed to the capping ability of EG,[53−55] which can coordinate with many cations.[36,50,52,56,57]

As is well-known, the morphology of MoS_2 affects the active-edges exposure directly. Therefore, a great diminution of active edges was caused by the oblique and further overlapping of MoS_2 nanosheets with water as solvent. On the other hand, lots of active edges were hidden in tiny nanospheres with EG as solvent. These inefficiently exposed active edges determined the poor HER performance in this system. Cathodes of MoS_2 on CC with water and EG as solvents show lower HER activity than MoS_2⊥CC (Figure 4d). Therefore, DMF is proved to be

DOI: 10.1021/acsami.5b02586
ACS Appl. Mater. Interfaces 2015, 7, 12193−12202

the appropriate solvent to guarantee effective exposure of active edges.

We further investigated the temperature effects at 180, 200, 220, and 240 °C, respectively. As shown in Figure 4e, at 180 °C, nanosheet-structure MoS_2 are sparser and less erect on CC than those synthesized through 200 °C (Figure 4a). This may be due to inadequate reduction of MoS_2 upon the relative low 180 °C.[15,18,20,58] In addition, MoS_2 synthesized at 220 °C look like tiny worms spread on the CC with a low height and small length (Figure 4f), and even smaller and lower at 240 °C (Figure 4g). As reported, increasing the solvothermal temperature accelerates the nucleation rate.[59] When nucleation is fast and a large number of nuclei are formed, there is limited reagent left for the growth at the same time.[60,61] As a consequence, MoS_2 obtained at 200 °C were erect and high naonosheets with great active edges exposed. According to Figure 4h, MoS_2⊥CC at 200 °C obtains the best HER efficiency.

The concentration of the precursor also affects the morphology and HER efficiency of MoS_2 on CC. The concentrations of precursor varied from 0.245, 0.49, 0.98 to 1.5 mg/mL; 0.245 mg/mL results in sparse and slant MoS_2 nanosheets overlapping each other, as Figure 4i shows. Compared with 0.98 mg/mL (Figure 4a), 0.49 mg/mL also achieves vertically aligned MoS_2 nanosheets but with lower density (Figure 4j). As reported, nucleation is mainly controlled by the solution concentration;[62] high concentration contributes to the increase of nucleation sites and the product density.[46−48] Furthermore, lower nucleation density brings growth forward to the neighbor sites, which means a slant morphology, whereas higher nucleation density contributes to the vertical growth on the substrate due to the limited space.[43] Therefore, denser and more erect MoS_2 nanosheets with an increasing loading of 0.12, 0.19, and 0.27 mg/cm^2 caused more active-edges exposure as the concentration increased from 0.245 to 0.98 mg/mL. However, a higher concentration of 1.5 mg/mL led to a slightly decreased loading of 0.23 mg/cm^2 with a morphology of less erect MoS_2 nanosheets in a smaller size (Figure 4k). This may be ascribed to the extremely high concentration which made the nucleation too concentrated and too fast to allow enough reagent or time to be involved in the growth procedure. It led to a smaller size and an uncontrollable growth procedure, thus less erect tiny nanosheets. Correspondingly, Figure 4l shows that MoS_2⊥CC synthesized with the concentration of 0.98 mg/mL achieves the highest HER efficiency due to the dense and vertical alignment of MoS_2 nanosheets, thus maximum active edges exposed.

Overall, the vertically aligned morphology obtained by using DMF, 200 °C, and a concentration of 0.98 mg/mL shows the best HER performance due to the maximum active-edges exposure. Furthermore, through the above analysis of the growth procedure of different morphologies, a potential growth mechanism of this outstanding cathode, MoS_2⊥CC, is presented as in the following. Due to the adsorption of $(NH_4)_2MoS_4$ to CC and the strong interaction between MoS_2 and carbon materials, $(NH_4)_2MoS_4$ was reduced to MoS_2 nanosheets, which tend to nucleate and anchor on the carbon fibers of CC by DMF.[16,18,28] Due to the proper saturated pressure of DMF, MoS_2 nanosheets are more apt to be erective on CC. Additionally, 200 °C as the moderate temperature for the reduction of MoS_2, helped them grew into thin and high MoS_2 nanosheets. The proper and relatively high concentration of 0.98 mg/mL led to dense nanosheets which vertically aligned in a limited space with great active sites exposed, as Scheme 1 illustrates. Overall, through controlling the solvent, temperature, and concentration, which can influence the nucleation and growth of MoS_2 nanosheets, vertical growth of MoS_2 on CC with maximum active edges exposed has be successfully synthesized with excellent HER activity.

Scheme 1. Schematic Illustration of the Vertical Growth Process of MoS_2 Nanosheets on the Surface of Carbon Cloth

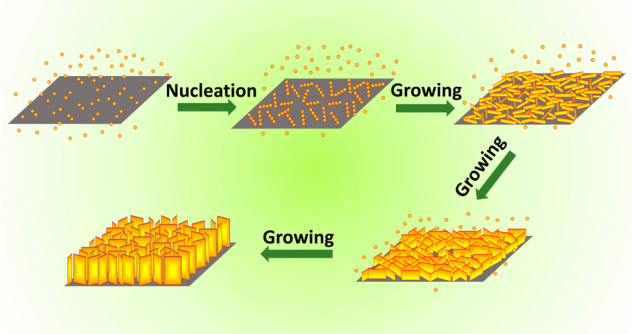

4. CONCLUSION

In conclusion, active-edges control of MoS_2 nanosheets grown on high conductive CC was realized by solvent and other conditions control during the solvothermal synthesis. Corresponding HER performances were measured to convince the realization of the active-edges control, and a comprehensive investigation of the growth mechanisms was pursued. This cathode with vertical and concentrated alignment of MoS_2 nanosheets on CC was proved to expose maximum active edges and achieve the outstanding HER performance in this investigation. The high density of active edges and excellent electron transfer efficiency were proved to contribute to the excellent HER activity, respectively. MoS_2⊥CC was also proved to possess good stability. This 3D flexible robust electrode exhibits preeminent HER activity with an onset overpotential of 100 mV and a Tafel slope of 39 mV per decade. Most importantly, the current density can reach 200 mA/cm^2 at 205 mV overpotential, which can rival the best MoS_2-based electrocatalysts ever reported.

■ ASSOCIATED CONTENT

Ⓢ Supporting Information

Additional figures giving detailed material characterizations and electrochemical measurements. The Supporting Information is available free of charge on the ACS Publications website at DOI: 10.1021/acsami.5b02586.

■ AUTHOR INFORMATION

Corresponding Author

*Tel: +86-0431-85262533. E-mail: tswu@ciac.ac.cn (T.W.).

Notes

The authors declare no competing financial interest.

■ ACKNOWLEDGMENTS

The authors are most grateful to the NSFC, China (Nos. 21205112, 21225524, 21475122, and 21127006), the Department of Science and Techniques of Jilin Province (Nos. 20120308, 201215091, and SYHZ0006), and the Chinese

DOI: 10.1021/acsami.5b02586
ACS Appl. Mater. Interfaces 2015, 7, 12193−12202

Academy of Sciences (Nos. YZ201354, YZ201355) for their financial support.

REFERENCES

(1) Dresselhaus, M. S.; Thomas, I. L. Alternative Energy Technologies. *Nature* **2001**, *414*, 332−337.

(2) Turner, J. A. Sustainable Hydrogen Production. *Science* **2004**, *305*, 972−974.

(3) Milliken, J.; Joseck, F.; Wang, M.; Yuzugullu, E. The Advanced Energy Initiative. *J. Power Sources* **2007**, *172*, 121−131.

(4) Sun, X.; Dai, J.; Guo, Y.; Wu, C.; Hu, F.; Zhao, J.; Zeng, X.; Xie, Y. Semimetallic Molybdenum Disulfide Ultrathin Nanosheets as an Efficient Electrocatalyst for Hydrogen Evolution. *Nanoscale* **2014**, *6*, 8359−8367.

(5) Toshima, N.; Yonezawa, T. Bimetallic Nanoparticles - Novel Materials for Chemical and Physical Applications. *New J. Chem.* **1998**, *22*, 1179−1201.

(6) Petrik, L. F.; Godongwana, Z. G.; Iwuoha, E. I. Platinum Nanophase Electro Catalysts and Composite Electrodes for Hydrogen Production. *J. Power Sources* **2008**, *185*, 838−845.

(7) Trasatti, S. Work Function, Electronegativity, and Electrochemical Behaviour of Metals. II. Potentials of Zero Charge and Electrochemical Work Functions. *J. Electroanal. Chem.* **1971**, *33*, 351−378.

(8) Benck, J. D.; Chen, Z.; Kuritzky, L. Y.; Forman, A. J.; Jaramillo, T. F. Amorphous Molybdenum Sulfide Catalysts for Electrochemical Hydrogen Production: Insights into the Origin of Their Catalytic Activity. *ACS Catal.* **2012**, *2*, 1916−1923.

(9) Xie, J.; Zhang, H.; Li, S.; Wang, R.; Sun, X.; Zhou, M.; Zhou, J.; Lou, X. W.; Xie, Y. Defect-Rich MoS_2 Ultrathin Nanosheets with Additional Active Edge Sites for Enhanced Electrocatalytic Hydrogen Evolution. *Adv. Mater.* **2013**, *25*, 5807−5813.

(10) Xie, J.; Zhang, J.; Li, S.; Grote, F.; Zhang, X.; Zhang, H.; Wang, R.; Lei, Y.; Pan, B.; Xie, Y. Controllable Disorder Engineering in Oxygen-Incorporated MoS_2 Ultrathin Nanosheets for Efficient Hydrogen Evolution. *J. Am. Chem. Soc.* **2013**, *135*, 17881−17888.

(11) Kibsgaard, J.; Chen, Z.; Reinecke, B. N.; Jaramillo, T. F. Engineering the Surface Structure of MoS_2 to Preferentially Expose Active Edge Sites for Electrocatalysis. *Nat. Mater.* **2012**, *11*, 963−969.

(12) Lukowski, M. A.; Daniel, A. S.; Meng, F.; Forticaux, A.; Li, L.; Jin, S. Enhanced Hydrogen Evolution Catalysis from Chemically Exfoliated Metallic MoS_2 Nanosheets. *J. Am. Chem. Soc.* **2013**, *135*, 10274−10277.

(13) Voiry, D.; Salehi, M.; Silva, R.; Fujita, T.; Chen, M.; Asefa, T.; Shenoy, V. B.; Eda, G.; Chhowalla, M. Conducting MoS_2 Nanosheets as Catalysts for Hydrogen Evolution Reaction. *Nano Lett.* **2013**, *13*, 6222−6227.

(14) Yan, Y.; Ge, X.; Liu, Z.; Wang, J.-Y.; Lee, J.-M.; Wang, X. Facile Synthesis of Low Crystalline MoS_2 Nanosheet-Coated CNTs for Enhanced Hydrogen Evolution Reaction. *Nanoscale* **2013**, *5*, 7768−7771.

(15) Li, Y.; Wang, H.; Xie, L.; Liang, Y.; Hong, G.; Dai, H. MoS_2 Nanoparticles Grown on Graphene: An Advanced Catalyst for the Hydrogen Evolution Reaction. *J. Am. Chem. Soc.* **2011**, *133*, 7296−7299.

(16) Ma, C.-B.; Qi, X.; Chen, B.; Bao, S.; Yin, Z.; Wu, X.-J.; Luo, Z.; Wei, J.; Zhang, H.-L.; Zhang, H. MoS_2 Nanoflower-Decorated Reduced Graphene Oxide Paper for High-Performance Hydrogen Evolution Reaction. *Nanoscale* **2014**, *6*, 5624−5629.

(17) Zhu, H.; Du, M.; Zhang, M.; Zou, M.; Yang, T.; Wang, S.; Yao, J.; Guo, B. S-Rich Single-Layered MoS_2 Nanoplates Embedded in N-Doped Carbon Nanofibers: Efficient Co-electrocatalysts for the Hydrogen Evolution Reaction. *Chem. Commun.* **2014**, *50*, 15435−15438.

(18) Zhao, X.; Zhua, H.; Yang, X. Amorphous Carbon Supported MoS_2 Nanosheets as Effective Catalysts for Electrocatalytic Hydrogen Evolution. *Nanoscale* **2014**, *6*, 10680−10685.

(19) Tenne, R.; Redlich, M. Recent Progress in the Research of Inorganic Fullerene-like Nanoparticles and Inorganic Nanotubes. *Chem. Soc. Rev.* **2010**, *39*, 1423−1434.

(20) Liao, L.; Zhu, J.; Bian, X.; Zhu, L.; Scanlon, M. D.; Girault, H. H.; Liu, B. MoS_2 Formed on Mesoporous Graphene as a Highly Active Catalyst for Hydrogen Evolution. *Adv. Funct. Mater.* **2013**, *23*, 5326−5333.

(21) Smith, A. J.; Chang, Y.-H.; Raidongia, K.; Chen, T.-Y.; Li, L.-J.; Huang, J. Molybdenum Sulfide Supported on Crumpled Graphene Balls for Electrocatalytic Hydrogen Production. *Adv. Energy Mater.* **2014**, *4*, 1400398−1400403.

(22) Youn, D. H.; Han, S.; Kim, J. Y.; Kim, J. Y.; Park, H.; Choi, S. H.; Lee, J. S. Highly Active and Stable Hydrogen Evolution Electrocatalysts Based on Molybdenum Compounds on Carbon Nanotube−Graphene Hybrid Support. *ACS Nano* **2014**, *8*, 5164−5173.

(23) Yao, Z.; Zhu, M.; Jiang, F.; Du, Y.; Wang, C.; Yang, P. Highly Efficient Electrocatalytic Performance Based on Pt Nanoflowers Modified Reduced Graphene Oxide/Carbon Cloth Electrode. *J. Mater. Chem.* **2012**, *22*, 13707−13713.

(24) Xu, J.; Wang, Q.; Wang, X.; Xiang, Q.; Hang, B.; Chen, D.; Shen, G. Flexible Asymmetric Supercapacitors Based upon Co_9S_8 Nanorod//Co_3O_4@RuO_2 Nanosheet Arrays on Carbon Cloth. *ACS Nano* **2013**, *7*, 5453−5462.

(25) Hou, X.; Wang, X.; Liu, B.; Wang, Q.; Luo, T.; Chen, D.; Shen, G. Hierarchical $MnCo_2O_4$ Nanosheet Arrays/Carbon Cloths as Integrated Anodes for Lithium-Ion Batteries with Improved Performance. *Nanoscale* **2014**, *6*, 8858−8864.

(26) Matte, H. S. S. R.; Gomathi, A.; Manna, A. K.; Late, D. J.; Datta, R.; Pati, S. K.; Rao, C. N. R. MoS_2 and WS_2 Analogues of Graphene. *Angew. Chem., Int. Ed.* **2010**, *49*, 4059−4062.

(27) Liu, C.-J.; Tai, S.-Y.; Chou, S.-W.; Yu, Y.-C.; Chang, K.-D.; Wang, S.; Chien, F. S.-S.; Lin, J.-Y.; Lin, T.-W. Facile Synthesis of MoS_2/Graphene Nanocomposite with High Catalytic Activity toward Triiodide Reduction in Dye-Sensitized Solar Cells. *J. Mater. Chem.* **2012**, *22*, 21057−21064.

(28) Deng, Z. H.; Li, L.; Ding, W.; Xiong, K.; Wei, Z. D. Synthesized Ultrathin MoS_2 Nanosheets Perpendicular to Graphene for Catalysis of Hydrogen Evolution Reaction. *Chem. Commun.* **2015**, *51*, 1893−1896.

(29) Romero-Rivera, R.; Camacho, A. G.; Del Valle, M.; Alonso, G.; Fuentes, S.; Cruz-Reyes, J. HDS of DBT with Molybdenum Disulfide Catalysts Prepared by in Situ Decomposition of Alkyltrimethylammonium Thiomolybdates. *Top. Catal.* **2011**, *54*, 561−567.

(30) Pu, Z.; Liu, Q.; Asiri, A. M.; Obaid, A. Y.; Sun, X. Graphene Film-Confined Molybdenum Sulfide Nanoparticles: Facile One-Step Electrodeposition Preparation and Application as a Highly Active Hydrogen Evolution Reaction Electrocatalyst. *J. Power Sources* **2014**, *263*, 181−185.

(31) Xu, K.; Wang, F.; Wang, Z.; Zhan, X.; Wang, Q.; Cheng, Z.; Safdar, M.; He, J. Component-Controllable $WS_{2(1-x)}Se_{2x}$ Nanotubes for Efficient Hydrogen Evolution Reaction. *ACS Nano* **2014**, *8*, 8468−8476.

(32) Wang, H.; Lu, Z.; Kong, D.; Sun, J.; Hymel, T. M.; Cui, Y. Electrochemical Tuning of MoS_2 Nanoparticles on Three-Dimensional Substrate for Efficient Hydrogen Evolution. *ACS Nano* **2014**, *8*, 4940−4947.

(33) Laursen, A. B.; Kegnaes, S.; Dahl, S.; Chorkendorff, I. Molybdenum Sulfides-Efficient and Viable Materials for Electro - and Photoelectrocatalytic Hydrogen Evolution. *Energy Environ. Sci.* **2012**, *5*, 5577−5591.

(34) Schweiger, H.; Raybaud, P.; Kresse, G.; Toulhoat, H. Shape and Edge Sites Modifications of MoS_2 Catalytic Nanoparticles Induced by Working Conditions: A Theoretical Study. *J. Catal.* **2002**, *207*, 76−87.

(35) Lauritsen, J. V.; Kibsgaard, J.; Helveg, S.; Topsoe, H.; Clausen, B. S.; Laegsgaard, E.; Besenbacher, F. Size-Dependent Structure of MoS_2 Nanocrystals. *Nat. Nanotechnol.* **2007**, *2*, 53−58.

DOI: 10.1021/acsami.5b02586
ACS Appl. Mater. Interfaces 2015, 7, 12193−12202

(36) Ghoshal, T.; Kar, S.; Chaudhuri, S. ZnO Doughnuts: Controlled Synthesis, Growth Mechanism, and Optical Properties. *Cryst. Growth Des.* **2007**, *7*, 136−141.
(37) Xu, L.; Hu, Y.-L.; Pelligra, C.; Chen, C.-H.; Jin, L.; Huang, H.; Sithambaram, S.; Aindow, M.; Joesten, R.; Suib, S. L. ZnO with Different Morphologies Synthesized by Solvothermal Methods for Enhanced Photocatalytic Activity. *Chem. Mater.* **2009**, *21*, 2875−2885.
(38) Hu, X.; Masuda, Y.; Ohji, T.; Kato, K. Low-Temperature Fabrication of Porous and Transparent ZnO Films with Hybrid Structure by Self-Hydrolysis Method. *Thin Solid Films* **2009**, *518*, 638−641.
(39) He, F.; Yang, P.; Niu, N.; Wang, W.; Gai, S.; Wang, D.; Lin, J. Hydrothermal Synthesis and Luminescent Properties of YVO_4:$Ln^{(3+)}$ (Ln = Eu, Dy, And Sm) Microspheres. *J. Colloid Interface Sci.* **2010**, *343*, 71−78.
(40) Lu, C. H.; Yeh, C. H. Influence of Hydrothermal Conditions on the Morphology and Particle Size of Zinc Oxide Powder. *Ceram. Int.* **2000**, *26*, 351−357.
(41) Kar, S.; Dev, A.; Chaudhuri, S. Simple Solvothermal Route To Synthesize ZnO Nanosheets, Nanonails, and Well-Aligned Nanorod Arrays. *J. Phys. Chem. B* **2006**, *110*, 17848−17853.
(42) Shi, W.; Zhou, L.; Song, S.; Yang, J.; Zhang, H. Hydrothermal Synthesis and Thermoelectric Transport Properties of Impurity-Free Antimony Telluride Hexagonal Nanoplates. *Adv. Mater.* **2008**, *20*, 1892−1897.
(43) Liu, B.; Aydil, E. S. Growth of Oriented Single-Crystalline Rutile TiO_2 Nanorods on Transparent Conducting Substrates for Dye-Sensitized Solar Cells. *J. Am. Chem. Soc.* **2009**, *131*, 3985−3990.
(44) Ghezelbash, A.; Koo, B.; Korgel, B. A. Self-Assembled Stripe Patterns of CdS Nanorods. *Nano Lett.* **2006**, *6*, 1832−1836.
(45) Zhang, G.; Wang, W.; Lu, X.; Li, X. Solvothermal Synthesis of V−VI Binary and Ternary Hexagonal Platelets: The Oriented Attachment Mechanism. *Cryst. Growth Des.* **2009**, *9*, 145−150.
(46) Lan, X.; Jiang, Y.; Su, H.; Li, S.; Wu, D.; Liu, X.; Han, T.; Han, L.; Qin, K.; Zhong, H.; Meng, X. Magnificent CdS Three-Dimensional Nanostructure Arrays: The Synthesis of a Novel Nanostructure Family for Nanotechnology. *CrystEngComm* **2011**, *13*, 145−152.
(47) Lopez, O. E.; Tucker, A. L.; Singh, K. R.; Mamer, S. B.; Sadoqi, M.; Xu, H. Synthesis of Zinc Oxide Nanowires on Seeded and Unseeded Gold Substrates: Role of Seed Nucleation and Precursor Concentration. *Superlattices Microstruct.* **2014**, *75*, 358−370.
(48) Kasamechonchung, P.; Horprathum, M.; Boonpavanitchakul, K.; Supaka, N.; Prompinit, P.; Kangwansupamonkon, W.; Somboonkaew, A.; Wetcharungsri, J.; Pratontep, S.; Porntheeraphat, S.; Klamchuen, A. Morphology-Controlled Seed-Assisted Hydrothermal ZnO Nanowires via Critical Concentration for Nucleation and Their Photoluminescence Properties. *Phys. Status Solidi A* **2015**, *212*, 394−400.
(49) Laursen, A. B.; Vesborg, P. C. K.; Chorkendorff, I. A High-Porosity Carbon Molybdenum Sulphide Composite with Enhanced Electrochemical Hydrogen Evolution and Stability. *Chem. Commun.* **2013**, *49*, 4965−4967.
(50) Liu, X. Y.; Zeng, J. H.; Zhang, S. Y.; Zheng, R. B.; Liu, X. M.; Qian, Y. T. Novel Bismuth Nanotube Arrays Synthesized by Solvothermal Method. *Chem. Phys. Lett.* **2003**, *374*, 348−352.
(51) Bai, Z.; Xu, P.; Chao, S.; Yan, H.; Cui, Q.; Niu, L.; Yang, L.; Qiao, J. A Facile One-Step Preparation of a Pd-Co Bimetallic Hollow Nanosphere Electrocatalyst for Ethanol Oxidation. *Catal. Sci. Technol.* **2013**, *3*, 2843−2848.
(52) Yang, J.; Li, C.; Quan, Z.; Zhang, C.; Yang, P.; Li, Y.; Yu, C.; Lin, J. Self-Assembled 3D Flowerlike Lu_2O_3 and Lu_2O_3:$Ln^{(3+)}$ (Ln = Eu, Tb, Dy, Pr, Sm, Er, Ho, Tm) Microarchitectures: Ethylene Glycol-Mediated Hydrothermal Synthesis and Luminescent Properties. *J. Phys. Chem. C* **2008**, *112*, 12777−12785.
(53) Feldmann, C. Polyol-Mediated Synthesis of Nanoscale Functional Materials. *Adv. Funct. Mater.* **2003**, *13*, 101−107.
(54) Wang, Y. L.; Jiang, X. C.; Xia, Y. N. A Solution-Phase, Precursor Route to Polycrystalline SnO_2 Nanowires That Can Be Used for Gas Sensing under Ambient Conditions. *J. Am. Chem. Soc.* **2003**, *125*, 16176−16177.
(55) Jiang, L. H.; Sun, G. Q.; Zhou, Z. H.; Sun, S. G.; Wang, Q.; Yan, S. Y.; Li, H. Q.; Tian, J.; Guo, J. S.; Zhou, B.; Xin, Q. Size-Controllable Synthesis of Monodispersed SnO_2 Nanoparticles and Application in Electrocatalysts. *J. Phys. Chem. B* **2005**, *109*, 8774−8778.
(56) Gao, Y. H.; Niu, H. L.; Zeng, C.; Chen, Q. W. Preparation and Characterization, of Single-Crystalline Bismuth Nanowires by a Low-Temperature Solvothermal Process. *Chem. Phys. Lett.* **2003**, *367*, 141−144.
(57) Geng, J.; Lv, Y.; Lu, D. J.; Zhu, J. J. Sonochemical Synthesis of $PbWO_4$ Crystals with Dendritic, Flowery and Star-like Structures. *Nanotechnology* **2006**, *17*, 2614−2620.
(58) Yuan, H.; Li, J.; Yuan, C.; He, Z. Facile Synthesis of MoS_2@CNT as an Effective Catalyst for Hydrogen Production in Microbial Electrolysis Cells. *ChemElectroChem* **2014**, *1*, 1828−1833.
(59) Thuy-Duong, N.-P.; Chinh, N.-H.; Shin, B. W. Morphological Evolution of Hierarchical Nickel Titanates by Elevation of the Solvothermal Temperature. *Mater. Lett.* **2014**, *131*, 217−221.
(60) Yanagisawa, K.; Ovenstone, J. Crystallization of Anatase from Amorphous Titania Using the Hydrothermal Technique: Effects of Starting Material and Temperature. *J. Phys. Chem. B* **1999**, *103*, 7781−7787.
(61) Diring, S.; Furukawa, S.; Takashima, Y.; Tsuruoka, T.; Kitagawa, S. Controlled Multiscale Synthesis of Porous Coordination Polymer in Nano/Micro Regimes. *Chem. Mater.* **2010**, *22*, 4531−4538.
(62) Lin, I. C.; Lo, H. J.; Song, S. R.; Fang, J. N.; Chen, Y. L.; Chen, H. F.; Li, L. J.; Liu, C. M. Controlling of Solution Concentration on Nucleation during Hydrothermal Synthesis of Analcime. *J. Chin. Chem. Soc.* **2002**, *49*, 495−498.
(63) Chen, Z.; Cummins, D.; Reinecke, B. N.; Clark, E.; Sunkara, M. K.; Jaramillo, T. F. Core−shell MoO_3−MoS_2 Nanowires for Hydrogen Evolution: A Functional Design for Electrocatalytic Materials. *Nano Lett.* **2011**, *11*, 4168−4175.
(64) Li, D. J.; Maiti, U. N.; Lim, J.; Choi, D. S.; Lee, W. J.; Oh, Y.; Lee, G. Y.; Kim, S. O. Molybdenum Sulfide/N-Doped CNT Forest Hybrid Catalysts for High-Performance Hydrogen Evolution Reaction. *Nano Lett.* **2014**, *14*, 1228−1233.
(65) Zheng, X.; Xu, J.; Yan, K.; Wang, H.; Wang, Z.; Yang, S. Space-Confined Growth of MoS_2 Nanosheets within Graphite: The Layered Hybrid of MoS_2 and Graphene as an Active Catalyst for Hydrogen Evolution Reaction. *Chem. Mater.* **2014**, *26*, 2344−2353.
(66) Zhou, W.; Zhou, K.; Hou, D.; Liu, X.; Li, G.; Sang, Y.; Liu, H.; Li, L.; Chen, S. Three-Dimensional Hierarchical Frameworks Based on MoS_2 Nanosheets Self-Assembled on Graphene Oxide for Efficient Electrocatalytic Hydrogen Evolution. *ACS Appl. Mater. Interfaces* **2014**, *6*, 21534−21540.
(67) Ge, X.; Chen, L.; Zhang, L.; Wen, Y.; Hirata, A.; Chen, M. Nanoporous Metal Enhanced Catalytic Activities of Amorphous Molybdenum Sulfide for High-Efficiency Hydrogen Production. *Adv. Mater.* **2014**, *26*, 3100−3104.
(68) Hou, Y.; Zhang, B.; Wen, Z.; Cui, S.; Guo, X.; He, Z.; Chen, J. A 3D Hybrid of Layered MoS_2/Nitrogen-Doped Graphene Nanosheet Aerogels: An Effective Catalyst for Hydrogen Evolution in Microbial Electrolysis Cells. *J. Mater. Chem. A* **2014**, *2*, 13795−13800.

DOI: 10.1021/acsami.5b02586
ACS Appl. Mater. Interfaces 2015, 7, 12193−12202